




Magnetically driven flow in a liquid-metal battery

P. A. Davidson,¹ O. Wong ,¹ J. W. Atkinson ,² and A. Ranjan ³

¹*Department of Engineering, University of Cambridge, Cambridge CB21PZ, United Kingdom*

²*British Antarctic Survey, Cambridge CB3 0ET, United Kingdom*

³*Department of Mechanical Engineering, IIT Bombay, Powai, Mumbai, Maharashtra 400076, India*



(Received 28 January 2022; accepted 6 June 2022; published 6 July 2022)

We investigate the flow within a liquid-metal battery induced by an externally imposed magnetic field, B_0 . An analytical model for laminar flow is proposed and this is found to be in excellent agreement with numerical simulations, not only for weakly forced steady flow, but also for the time-averaged velocity in more strongly forced flows where the motion is either unsteady (but laminar) or else weakly turbulent. Our primary conclusion is that surprisingly weak magnetic fields are capable of destabilizing the flow and inducing turbulence, with turbulence first appearing at $B_0 \approx 1.0$ G. By comparison, the earth's magnetic field is ~ 0.5 G. This extreme sensitivity of liquid-metal pools carrying current to an external magnetic field has long been known in the context of other industrial processes.

DOI: [10.1103/PhysRevFluids.7.074701](https://doi.org/10.1103/PhysRevFluids.7.074701)

I. INTRODUCTION

A. Liquid-metal batteries

The storage of energy from renewable sources is central to the effective use of wind and solar power. A variety of storage schemes have been tested, and the charging and discharging of batteries is one of the leading contenders. Different types of batteries have been developed for this purpose, including batteries in which the electrodes are liquid metals, so called liquid-metal batteries (LMBs). A typical geometry is shown in Fig. 1(a). Two liquid metals of different electropotential (say, lithium and an alloy of bismuth) are separated by an electrolyte. Current passes up or down through the three fluid layers, depending on whether the battery is charging or discharging. In the case of discharge, the current passes down through the three liquids and then into the base of the outer steel shell, which acts both as a container and as a current collector.

An alternative design, which is the focus of this paper, is shown in Fig. 1(b). Here the lithium is immobilized within a steel matrix and current passes down through the lithium matrix, across the electrolyte and into the bismuth pool, and finally into the steel shell that encloses the battery. In this design most of the current in the bismuth flows radially outward to the sides of the container, rather than downward to its base. Notice that the electrolyte layer is thin in both designs, which is essential because it has a high electrical resistivity. That is to say, to maintain a competitive energy efficiency for the charge-discharge cycle, the electrolyte thickness cannot exceed a few millimeters for practical battery sizes.

Because of their commercial importance, there have been many studies of the fluid mechanics of LMBs, most of which are discussed in the extensive review in [1]. This includes both electromagnetic and buoyancy-driven flows (see, e.g., [2]). More recent papers that focus particularly on electromagnetically driven flows include [3–6]. These differ primarily in their geometries and the means of collecting the current.

A recent development, driven by the need for the scale-up of storage capacity, has been the clustering of batteries into closely packed groups, with current passing from battery to battery within

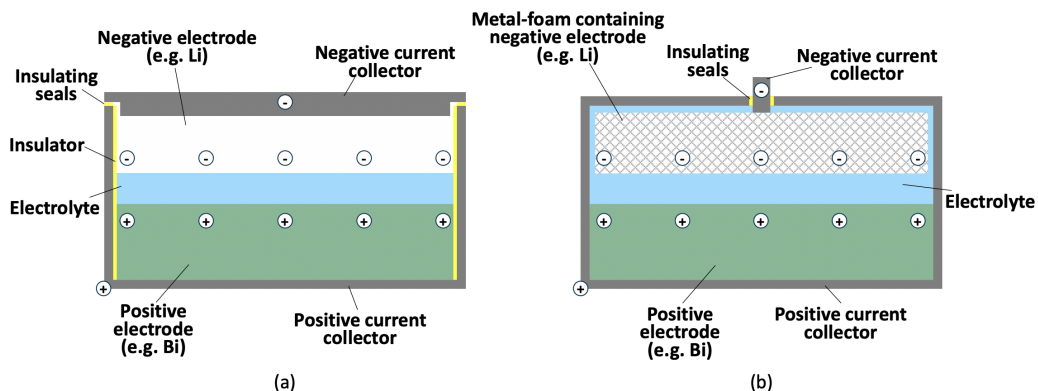


FIG. 1. Schematic of a liquid-metal battery. (a) A simple design. (b) An alternative design.

a given cluster. This is significant as the magnetic field generated by the connecting wires within a cluster can interact with the current passing through a given battery to drive flow within that battery. While some motion is beneficial for mixing (see [5]), too much can produce strong turbulence which may disrupt the interface with the thin electrolyte layer. For the battery in Fig. 1(b), the most important external magnetic field is a vertical one, as this interacts with the radial current to give an azimuthal Lorentz force. This, in turn, drives a swirling flow within the bismuth. The main purpose of this paper is to investigate the flow driven by just such an external, vertical magnetic field. We build on the study reported in [5].

B. Simple model of a liquid-metal battery

Our model of a cylindrical lithium-bismuth liquid-metal battery is shown in Fig. 2. As in [5], it is axisymmetric and we adopt cylindrical polar coordinates (r, θ, z) , centered on the base of the battery. Current enters through the central stub, passes down into the lithium matrix and then into the bismuth, and is finally collected in the outer steel shell, predominantly at the cylindrical sidewall. The fluid interface between the electrolyte and bismuth is taken to be steady, and we suppose that there is a uniform external magnetic field of $\mathbf{B} = -B_0 \hat{\mathbf{e}}_z$. In the interests of simplicity, we take the annular gap between the lithium electrode and the container wall, which is filled with electrolyte, to be the same width as the container shell, T . Our benchmark case is documented in Table I. Note that the depth of the bismuth may vary from design to design (cf. [7]), but our model is insensitive to this depth, provided it exceeds the boundary layer thickness.

Note that there are two magnetic fields, and hence two Lorentz forces acting on the bismuth. On the one hand, there is an azimuthal magnetic field, B_θ , associated directly with the flow of

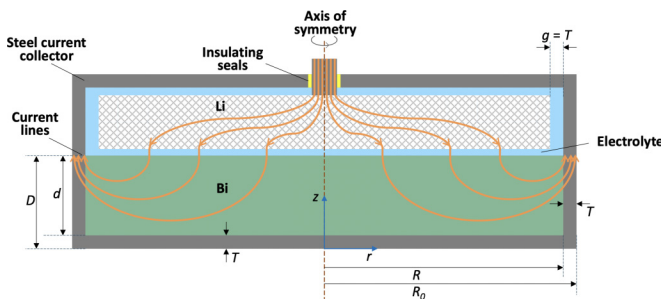


FIG. 2. Our model of a liquid-metal battery.

TABLE I. Benchmark case. The dimensions are defined in Fig. 2. ρ is density, ν viscosity, σ electrical conductivity. (Properties from [5,1].)

Dimensions	$R_0 = R + T = 10$ cm, $R = 9$ cm, $D = d + T = 4$ cm, $d = 2w = 3$ cm, $g = T = 1$ cm
Bi at 500 °C	$\rho = 9720$ kg/m ³ , $\nu = 1.2 \times 10^{-7}$ m ² /s, $\sigma = 7.3 \times 10^5$ S/m
Battery current	$I = 100$ A (or equivalently, $J = 0.393$ A/cm ²)

current through the battery. This interacts with the current density, \mathbf{J} , to give rise to a poloidal Lorentz force per unit mass, $\mathbf{J} \times \mathbf{B}/\rho$, which drives flow in a vertical plane. On the other hand, the external magnetic field, $\mathbf{B} = -B_0 \hat{\mathbf{e}}_z$, interacts with \mathbf{J} to drive a horizontal swirling flow (and its associated Ekman pumping in the vertical plane). However, it is well known that, provided $|B_z|$ exceeds $\sim 0.01B_\theta$, the fluid motion is completely dominated by the Lorentz force associated with the external magnetic field (see [8], Fig. 12.9 in [9], or [10]). For a battery current of 100 A, we expect $B_\theta \sim 2$ G, whereas we shall consider external magnetic fields in the range $|B_z| = 0.5 \rightarrow 1.5$ G. Clearly we satisfy $|B_z| \gg 0.01B_\theta$, and so we are free to neglect the Lorentz force associated with B_θ .

II. ELECTROMAGNETIC FORCE DISTRIBUTION

A. Current distribution

Our first task is to calculate the flow of current down through the bismuth and back up through the metal container, which acts as a current collector. Actually, it turns out that the induced flow is rather insensitive to the precise distribution of the current density, \mathbf{J} , within the bismuth. The key point is that, as we shall see, the flow within the battery is largely (but not entirely) controlled by the *net* electromagnetic torque acting on the bismuth, and somewhat insensitive to the exact distribution of the Lorentz force. Moreover, we shall show that the net electromagnetic torque is simply controlled by the externally applied magnetic field and the current distribution at the surface of the bismuth. In short, the flow is more or less determined by B_0 and by the current entering the bismuth, and it is not sensitive to the exact distribution of \mathbf{J} *within* the bismuth. Nevertheless, it is useful to calculate the distribution of \mathbf{J} , if only to get the surface current distribution. In doing so, we make one small simplification. The electrical conductivities of the steel container and liquid bismuth are likely to differ by no more than around 10%–20%, whereas the conductivity of the electrolyte is a factor of 2500 times smaller than that of the bismuth. Therefore, in order to keep the algebra to a minimum, we take the electrical conductivity of the container wall to be the same as that of the bismuth.

The magnetic diffusion time in a liquid-metal battery is much less than the timescale of the motion, and so we may use the low magnetic Reynolds number approximation in which \mathbf{J} is treated as quasistatic and described by an electrostatic potential, $\mathbf{J} = -\sigma \nabla \varphi$, where σ is the electrical conductivity and φ the potential. Since \mathbf{J} is solenoidal, φ is harmonic, i.e., $\nabla^2 \varphi = 0$. Moreover, since \mathbf{J} is axisymmetric, it may be expressed in terms of a Stokes stream function, $\Psi(r, z)$. Combining these two statements, we have

$$\mathbf{J} = \nabla \times [(\Psi/r)\hat{\mathbf{e}}_\theta] = -\sigma \nabla \varphi, \quad \nabla^2 \varphi = 0, \quad (1)$$

where we use cylindrical polar coordinates (r, θ, z) , centered on the base of the container. This must be solved in the cylindrical domain $r \leq R_0$, $0 \leq z \leq D$, which comprises the bismuth and container wall (see Fig. 2).

The boundary conditions are straightforward. We take $\mathbf{J} \cdot \mathbf{n} = 0$ or, equivalently, $\Psi = 0$, along the boundaries $z = 0$ and $r = R_0$, and specify the variation in potential across the upper boundary $z = D$. Moreover, we shall take the simplest possible distribution for φ across the surface $z = D$, which is determined as follows. First we note that, since the electrolyte is much more resistive than the bismuth, the flow of current through the electrolyte from the base of the lithium electrode to the bismuth surface below is purely vertical. This means that the surface potential of the bismuth

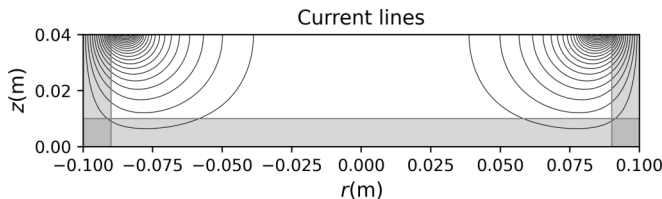


FIG. 3. The current distribution for our benchmark case. Note that very little of the current passes through the base of the container.

immediately below the lithium electrode will be uniform, say, $\varphi = V$ for $r < (R-T)$. We shall also take $\varphi = 0$ within the container wall, $R < r < R_0$, and assume a linear variation of φ in the annular gap in between, i.e., $\varphi = (R-r)V/T$ in the annulus $(R-T) < r < R$.

The solution of (1) which satisfies $\Psi = 0$ along the boundaries $z = 0$ and $r = R_0$ is readily shown to be

$$\Psi = -\sigma r \sum A_n J_1(\delta_n r/R_0) \sinh(\delta_n z/R_0), \quad (2)$$

$$\varphi = \sum A_n J_0(\delta_n r/R_0) \cosh(\delta_n z/R_0), \quad (3)$$

where J_0 and J_1 are the usual Bessel functions, δ_n is the n th zero of J_1 , and the coefficients A_n are chosen to satisfy the potential distribution $\varphi = Vf(r)$ across the surface $z = D$. Since $J_0(\delta_m r/R_0)$ and $J_0(\delta_n r/R_0)$ are orthogonal in $0 < r < R_0$ for $m \neq n$, (3) yields

$$A_n \cosh(\delta_n D/R_0) \int_0^{R_0} J_0^2(\delta_n r/R_0) r dr = V \int_0^{R_0} f(r) J_0(\delta_n r/R_0) r dr. \quad (4)$$

For our choice of $f(r)$, the integrals in (4) are all standard and catalogued in [11]. Consequently, it is readily confirmed that

$$A_n = \frac{2VR\tilde{J}_1(n)}{R_0\delta_n J_0^2(\delta_n) \cosh(\delta_n D/R_0)}, \quad (5)$$

where $\tilde{J}_1(n)$ is defined as

$$\tilde{J}_1(n) = \frac{1}{RT} \int_{R-T}^R r J_1(\delta_n r/R_0) dr. \quad (6)$$

The current density may be calculated from Ψ using (1), and the distribution of current for our benchmark case is shown in Fig. 3. Notice that nearly all of the current passes through the sidewall of the container and very little through the base. Of particular interest is the net current passing through the battery, which is given by

$$I_{\text{net}} = \int_0^R |J_z| 2\pi r dr = -2\pi \Psi(r=R) = \frac{4\pi\sigma VR^2}{R_0} \sum_n \frac{\tilde{J}_1(n) J_1(\delta_n R/R_0)}{\delta_n J_0^2(\delta_n)} \tanh\left(\frac{\delta_n D}{R_0}\right), \quad (7)$$

where J_z and Ψ are evaluated on $z = D$. For our benchmark case, this becomes

$$I_{\text{net}} = \gamma \frac{4\pi\sigma VR^2}{R_0}, \quad \gamma = 0.314, \quad (8)$$

which relates the current through the battery to the voltage drop across the bismuth.

B. Force distribution and net torque

The radial current density interacts with the external magnetic field, $\mathbf{B} = -B_0\hat{\mathbf{e}}_z$, to give rise to an azimuthal Lorentz force acting on the bismuth. From (2), this force is

$$F_\theta(r, z) = \frac{1}{\rho} J_r B_0 = -\frac{B_0}{\rho r} \frac{\partial \Psi}{\partial z} = \frac{2\sigma V B_0}{\rho} \frac{R}{R_0^2} \sum_n \frac{\tilde{J}_1(n) J_1(\delta_n r/R_0)}{J_0^2(\delta_n)} \frac{\cosh(\delta_n z/R_0)}{\cosh(\delta_n D/R_0)} \quad (9)$$

per unit mass. We shall see in Sec. III that the azimuthal flow is controlled by the depth-averaged force only, and that the z dependence of F_θ is unimportant. This depth-averaged force is, evidently,

$$\bar{F}_\theta(r) = \frac{2\sigma V B_0}{\rho} \frac{R}{2wR_0} \sum_n \frac{\tilde{J}_1(n) J_1(\delta_n r/R_0)}{\delta_n J_0^2(\delta_n)} \frac{\sinh(\delta_n D/R_0) - \sinh(\delta_n T/R_0)}{\cosh(\delta_n D/R_0)}. \quad (10)$$

Of particular interest is the net torque applied to the bismuth. From (9) this can be written as

$$T_{\text{net}} = \int r F_\theta \rho dV = B_0 \int_0^R [\Psi_{z=T} - \Psi_{z=H}] 2\pi r dr = B_0 \int_0^R [I_t(r) - I_b(r)] r dr, \quad (11)$$

where $I_t(s)$ is the current entering the top of the bismuth through the circle $r < s$, and $I_b(s)$ is the current exiting the bottom of the bismuth through the same circle. However, it is clear from Fig. 3 that $I_b(r) \approx 0$, and so

$$T_{\text{net}} \approx B_0 \int_0^R I_t(r) r dr. \quad (12)$$

Thus, as claimed above, the net torque is more or less controlled by B_0 and by the current at the surface of the bismuth. In terms of the Bessel function expansion, (9), the torque is

$$T_{\text{net}} = 4\pi\sigma V B_0 R^3 \sum_n \frac{\tilde{J}_1(n) J_2(\delta_n R/R_0)}{\delta_n^2 J_0^2(\delta_n)} \frac{\sinh(\delta_n D/R_0) - \sinh(\delta_n T/R_0)}{\cosh(\delta_n D/R_0)}, \quad (13)$$

and for our benchmark case, this becomes $T_{\text{net}} = 4\pi\kappa\sigma V B_0 R^3$, where $\kappa = 0.0594$. As suggested above, we shall find that the peak azimuthal velocity is largely controlled by this net torque.

A power-law approximation to (10) that yields the same net torque is, evidently,

$$\bar{F}_\theta(r) = \frac{T_{\text{net}}}{4\pi\rho R^3 w} (p+1)(r/R)^{p-2}. \quad (14)$$

For our benchmark case, this is a plausible approximation to (10) provided that we take $p = 6$, as shown in Fig. 4. We shall see that almost identical azimuthal flows are produced by the true force distribution, Eq. (9); its depth-average equivalent, Eq. (10); and the power-law approximation, Eq. (14), provided we use $p = 6$.

III. ANALYTICAL MODEL FOR STEADY LAMINAR FLOW

An approximate analytical solution to the problem of liquid-metal flow in an axisymmetric cavity, driven by an azimuthal Lorentz force, is given in [12]. We shall adapt and simplify that solution in a manner appropriate to a liquid-metal battery, using cylindrical polar coordinates (r, θ, z) . Because the electrolyte layer is very thin, we shall model the flow as a single fluid (bismuth) in a cylindrical container of height $2w$ and radius R , subject to no-slip boundary conditions at the top and bottom of the domain and at the sidewall $r = R$. Since the container wall is no longer relevant, it is convenient to now shift the origin of coordinates upward by a distance T , so that it lies at the bottom of the bismuth.

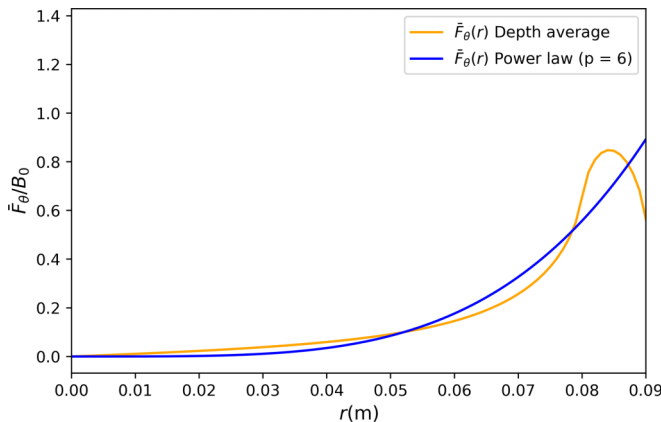


FIG. 4. A comparison of the depth-average force distribution of Eq. (10) (yellow) and power-law approximation (14) (blue), with $p = 6$, for the benchmark case.

Axisymmetric flow is often best described using the azimuthal components of the Navier-Stokes and vorticity equations, which are

$$\frac{D\Gamma}{Dt} = rF_\theta + \nu \nabla_*^2 \Gamma, \quad \Gamma = ru_\theta, \quad (15)$$

$$\frac{D}{Dt} \left(\frac{\omega_\theta}{r} \right) = \frac{\partial}{\partial z} \left(\frac{\Gamma^2}{r^4} \right) + \frac{\nu}{r^2} \nabla_*^2 (r\omega_\theta), \quad (16)$$

where ω_θ is the curl of the poloidal velocity $(u_r, 0, u_z)$, and ∇_*^2 is the axisymmetric Stokes operator, defined by

$$\nabla_*^2(\sim) = \left[r \frac{\partial}{\partial r} \frac{1}{r} \frac{\partial}{\partial r} + \frac{\partial^2}{\partial z^2} \right](\sim). \quad (17)$$

(See, for example, [13], Chap. 2.) If the flow is steady, then outside the boundary layers these reduce to

$$\mathbf{u} \cdot \nabla \Gamma = rF_\theta, \quad (18a)$$

$$\mathbf{u} \cdot \nabla \left(\frac{\omega_\theta}{r} \right) = \frac{\partial}{\partial z} \left(\frac{\Gamma^2}{r^4} \right). \quad (18b)$$

The overall structure of the flow is shown schematically in Fig. 5. There is an inviscid core flow bounded top and bottom by Bödewadt-like Ekman layers, and by a Stewartson boundary layer on the sidewall. The primary flow is azimuthal, $u_\theta = \Omega(r, z)r$, but the Ekman layers induce a secondary flow in the vertical plane, as shown in Fig. 5. This secondary flow is radially inward within the Ekman layers and outward within the inviscid core flow, with the Stewartson layers acting to recycle the flow at the sidewall. Laminar Ekman layers have a characteristic thickness of $\delta \sim \sqrt{\nu/\Omega}$ and they detrain mass at a rate of $|u_z| \sim \sqrt{\nu\Omega}$, say, $|u_z| = \alpha\sqrt{\nu\Omega}$ for some α of order unity. Indeed, for the idealized case where the Ekman layers are of infinite radial extent and the core flow is in a state of rigid body rotation, we have $\alpha = 1.350$. (See, e.g., [13], Chap. 10.)

A global torque balance requires that the net viscous torque exerted by the boundaries on the fluid, T_v , balances the applied Lorentz torque, $T_v = T_{\text{net}}$. Moreover, we might expect T_v to be dominated by the maximum angular momentum in the core, Γ_{max} , and by the associated boundary

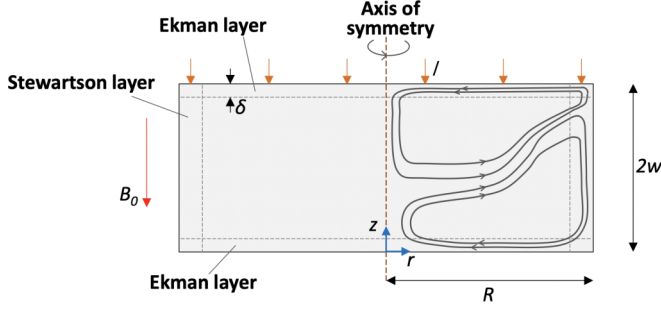


FIG. 5. The overall structure of the secondary flow.

layer thickness, $\delta \sim \sqrt{\nu R^2 / \Gamma_{\max}}$. We might anticipate, therefore, that Γ_{\max} is more or less fixed by the net Lorentz torque, T_{net} . We shall see shortly that this is indeed the case.

Note that in the Stewartson boundary layer the angular momentum, Γ , decreases with increasing radius. Hence the sidewall boundary layer tends to be unstable to Rayleigh's centrifugal instability, and in the case of unforced, spin-down experiments, this instability occurs when the Ekman number, $\text{Ek} = \nu / \Omega R^2$, falls below $\text{Ek} \sim 3 \times 10^{-3}$ (see [14]). However, [14] notes that the time-averaged flow in a turbulent spin-down experiment looks remarkably similar to the flow in the equivalent laminar experiment. So our laminar analysis may still be relevant to unsteady or turbulent flow.

The analytical model of [12] starts by noting that the angular momentum, Γ , in the inviscid core is independent of z , $\Gamma_c = \Gamma_c(r)$, at least to leading order in Ek. (The subscript c stands for "core".) The point is that, within the inviscid core flow, the magnitude of the secondary flow is set by the rate at which the Ekman layers detrain mass, $u_r \sim u_z \sim \sqrt{\nu \Omega}$. Equation (18b) then demands

$$\frac{\partial \Gamma_c^2}{\partial z} = r^4 \mathbf{u} \cdot \nabla \left(\frac{\omega_\theta}{r} \right) \sim r^4 u_r \frac{\partial}{\partial r} \frac{1}{r} \frac{\partial u_r}{\partial z} \sim \frac{r^2 u_r^2}{w} \sim \frac{\nu \Gamma}{w}, \quad (19)$$

and so $\partial \Gamma_c / \partial z \sim \nu / w$. Thus, within the core, $\partial \Gamma_c / \partial z \approx 0$ to leading order in Ek. Davidson [12] then determines the overall flow structure for an axisymmetric cavity of arbitrary shape through a consideration of the Ekman layers. However, we shall take advantage of the simple cylindrical geometry in Fig. 5 to develop a different approach, one that allows us to sidestep a detailed consideration of the Ekman layers. Substituting $\Gamma_c = \Gamma_c(r)$ into (18a) yields

$$u_r \frac{d\Gamma_c}{dr} = r F_\theta,$$

from which

$$2\pi r \int_\delta^{2w-\delta} u_r dz \frac{d\Gamma_c}{dr} = 2\pi r^2 \int_\delta^{2w-\delta} F_\theta dz = 4\pi w r^2 \bar{F}_\theta(r), \quad (20)$$

to leading order in Ek. Let $u_b(r)$ be the magnitude of the axial velocity at the edge of the Ekman layers, with $u_b = \alpha \sqrt{\nu \Omega}$. Then we can use continuity to rewrite (20) as

$$2 \int_0^r 2\pi r u_b dr \frac{d\Gamma_c}{dr} = 4\pi w r^2 \bar{F}_\theta(r), \quad (21)$$

or, equivalently,

$$\alpha \sqrt{\nu} \frac{d\Gamma_c}{dr} \int_0^r \Gamma_c^{1/2} dr = w r^2 \bar{F}_\theta(r). \quad (22)$$

This is the key equation that determines the distribution of angular momentum in the inviscid core. For simplicity, we shall take the infinite disk value for α , of $\alpha = 1.350$.

Perhaps some comments are in order. First, as claimed above, Γ_c is determined by the depth-averaged force distribution, and so the z dependence of $F_\theta(r, z)$ is irrelevant as far as u_θ is concerned. Second, for the case where $\bar{F}_\theta(r)$ is approximated by a power law,

$$\bar{F}_\theta(r) = \frac{T_{\text{net}}}{4\pi\rho R^3 w} (p+1)(r/R)^{p-2},$$

equation (22) gives us

$$\Gamma_c(r) = \left(\frac{\lambda_p T_{\text{net}}}{\pi\alpha R\rho\sqrt{v}} \right)^{2/3} \left(\frac{r}{R} \right)^{2p/3}, \quad \lambda_p = \frac{(3+p)(p+1)}{8p}. \quad (23)$$

Thus, for a given value of p , the maximum value of Γ is fixed by the net Lorentz torque, as suggested above. Third, we can use (11) to rewrite (22) in terms of the current passing through the top surface of the bismuth, as well as that which leaves at the base of the bismuth layer. The end result is

$$\frac{d\Gamma_c}{dr} \int_0^r \Gamma_c^{1/2} dr = \frac{B_0 r [I_t(r) - I_b(r)]}{4\pi\alpha\rho\sqrt{v}} \approx \frac{B_0 r I_t(r)}{4\pi\alpha\rho\sqrt{v}}, \quad (24)$$

which emphasises the importance of the surface current distribution in controlling the flow. Fourth, (22) and (24) integrate to give

$$\int_0^R \Gamma_c^{1/2} [\Gamma_c(R) - \Gamma_c(r)] dr = \frac{T_{\text{net}}}{4\pi\alpha\rho\sqrt{v}} = \frac{B_0}{4\pi\alpha\rho\sqrt{v}} \int_0^R [I_t(r) - I_b(r)] r dr, \quad (25)$$

which again highlights the importance of T_{net} and $I_t(r)$ as the controlling parameters. Finally, it is clear from (24) and (25) that the azimuthal velocity scales as

$$u_\theta \sim V_B (V_B R / \nu)^{1/3}, \quad V_B = \sqrt{I_{\text{net}} B_0 / 4\pi R \rho}, \quad (26)$$

where V_B is the characteristic velocity of the induced flow. This may also be written as

$$u_\theta \sim F_\theta^{2/3} R / \nu^{1/3}, \quad (27)$$

where the two-thirds scaling law has long been known to be a consequence of a balance between laminar Ekman pumping and an applied azimuthal Lorentz force (see [12], or [9], Sec. 6.4.2).

IV. NUMERICAL SIMULATIONS OF THE FLOW

A. Numerical scheme

Numerical simulations were performed using the open-source computational fluid dynamics software OPENFOAM 7 running a modified version of the ICOFOAM solver [15]. This is an implementation of the PISO (pressure implicit with splitting of operators) algorithm for solving the Navier-Stokes equations [16]. The code was modified to include the azimuthal Lorentz force as a body force, with the option of the three different formulations given in Eqs. (9), (10), and (14). As noted earlier, these expressions are quite general and are limited only by the assumption that the bismuth and container wall have the same electrical conductivity.

A regular cylindrical mesh of 1 325 520 cells was used with refinement near the upper and lower surfaces and at the radial boundary. The mesh was also checked for skewness. Grid independence checks were carried out by increasing the mesh resolution while ensuring the results for the largest field strengths (i.e., largest Reynolds numbers) remained unchanged. Time stepping was performed using the second-order Crank-Nicolson scheme. Step independence was checked by decreasing the time step and ensuring that the time evolution of global variables remained unaffected.

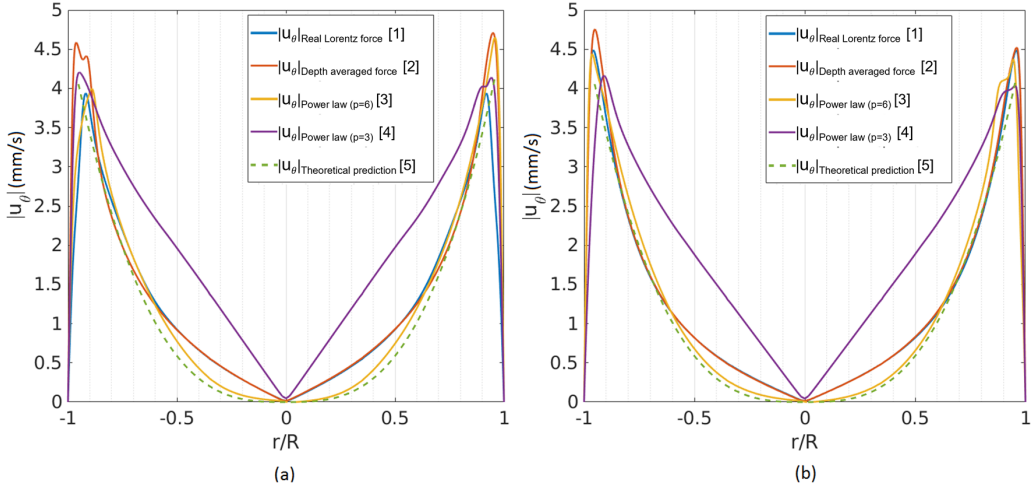


FIG. 6. The instantaneous azimuthal velocity for the case of $B_0 = 0.5$ G at $t = 2500$ s: (a) $z/d = 0.23$; (b) midplane ($z/d = 0.5$). The flow is computed for the applied forces: full force distribution [Eq. (9), curve 1, blue]; depth averaged [Eq. (10), curve 2, red]; power-law approximation [Eq. (14)] with $p = 6$ (curve 3, yellow) and $p = 3$ (curve 4, purple). The theoretical prediction of Eq. (23) with $p = 6$ is plotted in curve 5 (green, dashed).

The dimensions of the domain and physical properties of the fluid are given in Table I for all simulations. Several values of the external magnetic field were chosen in the range 0.1–1.5 G. The boundary conditions are the same as those presented in Sec. III, no-slip at the upper, lower, and radial boundaries. All simulations were run from a stationary state of $\mathbf{u} = 0$. As such, the results display initial transients during spin-up before reaching a statistically steady state. This final state might be steady, show regular oscillations, or be weakly turbulent with steady global properties, depending on the value of B_0 .

B. Results of the simulations for $B_0 = 0.5$ G

We now describe the results of a series of numerical experiments all performed for our benchmark geometry (see Table I) and for a battery current of 100 A. The only parameter that changes from

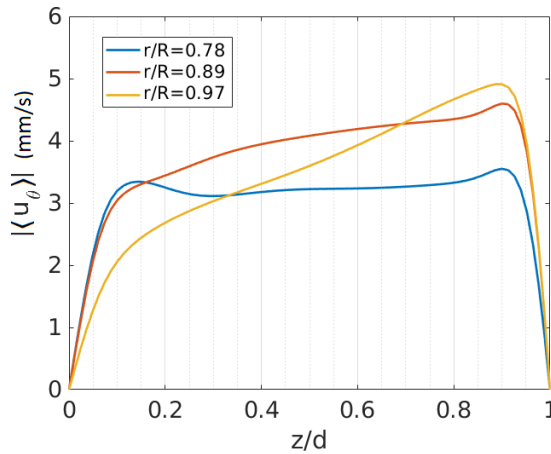


FIG. 7. Variation of the time-averaged u_θ with vertical position for $B_0 = 0.5$ G, at $r/R = 0.78, 0.89, 0.972$. The symbol $\langle \rangle$ denotes a time average.

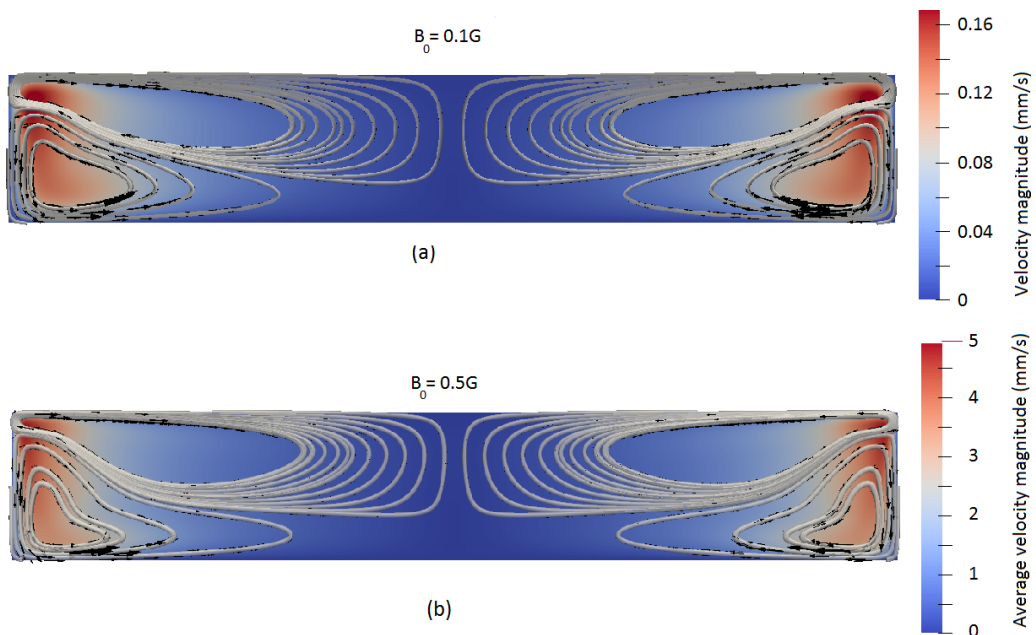


FIG. 8. (a) The instantaneous velocity magnitude, $|\mathbf{u}|$, and streamlines in a vertical plane, for $B_0 = 0.1\text{ G}$ at $t = 1000\text{ s}$. (b) The time-averaged velocity magnitude, and streamlines showing the time-averaged poloidal flow, for $B_0 = 0.5\text{ G}$.

simulation to simulation is the external magnetic field, B_0 . This is increased from 0.5 G, which is more or less the intensity of the terrestrial magnetic field, up to 1.5 G, which is the magnetic field generated by a wire carrying a current of 100 A at a distance of 13 cm. By comparison, the stray magnetic field generated by the interconnections within a battery cluster is likely to be of the order of 1 or 2 G, provided the batteries are all connected in series.

The computed flows for $B_0 \leq 0.8\text{ G}$ are laminar but unsteady, whereas for $B_0 \geq 1\text{ G}$ they are weakly turbulent, as discussed below. In this section we focus on the case of $B_0 = 0.5\text{ G}$. Figure 6 shows a snapshot of the azimuthal velocity at $z/d = 0.23$ and on the midplane for the case of $B_0 = 0.5\text{ G}$. Curve 1 is the computed flow generated by the actual Lorentz force [Eq. (9)], curve 2 the flow generated by the equivalent depth-averaged force [Eq. (10)], curves 3 and 4 are the flows generated by the power-law approximation to the depth-averaged force distribution [Eq. (14), for $p = 6$ and $p = 3$], and curve 5 the theoretical prediction [Eq. (23), with $p = 6$].

Recall that Eq. (14) with $p = 6$ is a reasonable approximation to the actual depth-averaged force distribution, while Eq. (14) with $p = 3$ is a poor approximation to the depth-averaged force, but does at least impose the correct net torque. It is clear that the flows generated by the actual force distribution, the depth-averaged force distribution, and the power-law approximation to the depth-averaged force distribution (with $p = 6$), all generate very similar azimuthal velocities at both heights. Moreover, our theoretical estimate for the core velocity, which is based on the power-law approximation to the depth-averaged force (with $p = 6$), is in excellent agreement with the corresponding computed flow. The only curve which deviates significantly from the others is the flow generated by the power-law, depth-averaged force with $p = 3$. Of course, this is no surprise since $p = 3$ is not a good approximation to the actual depth-averaged force distribution. Interestingly, though, the computed peak velocity for the $p = 3$ case is similar to that found with the other force distributions. This is because the net applied torque is the same in all cases, and the global torque balance, $T_v = T_{\text{net}}$, demands the peak velocity is more or less fixed by the net torque, as noted above. Also, the fact that the curves are similar for both heights suggests that the core

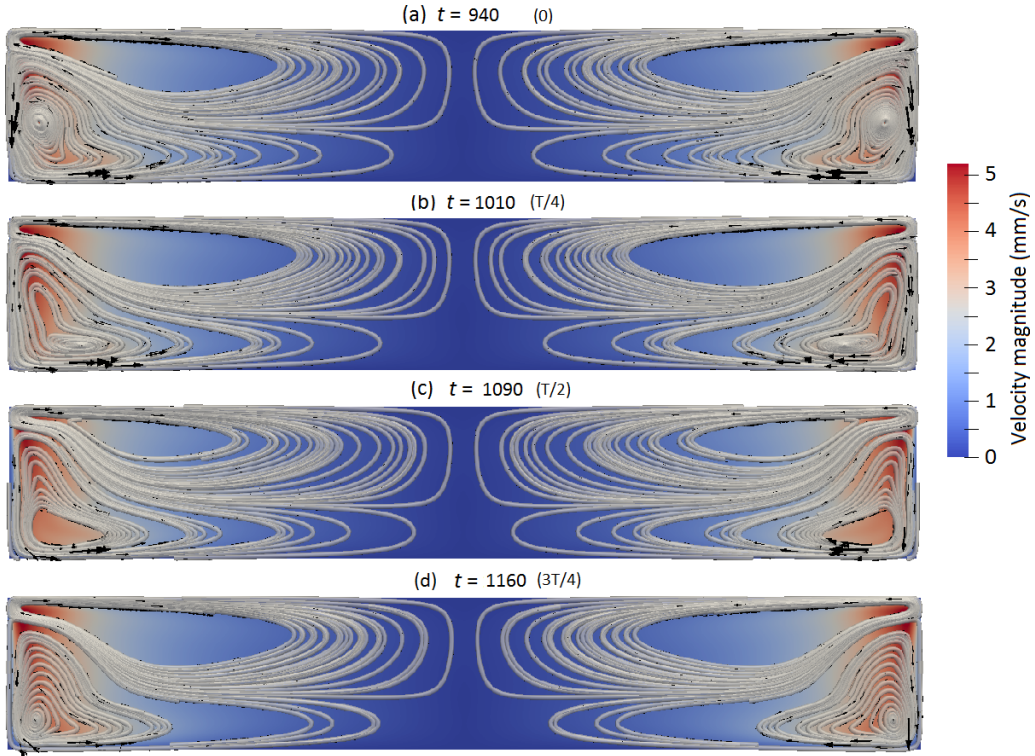


FIG. 9. The instantaneous velocity magnitude, $|\mathbf{u}|$, and streamlines in a vertical plane, for $B_0 = 0.5$ G at times (a) $t = 940$ s, (b) $t = 1010$ s, (c) $t = 1090$ s, and (d) $t = 1160$ s.

angular momentum is almost independent of depth, as predicted. This is confirmed in Fig. 7, which shows the variation of u_θ with z for the flow driven by the true force distribution, Eq. (9).

In the remainder of this section we consider only flows driven by the true force distribution, (9). The time-averaged streamlines in the vertical plane for $B_0 = 0.5$ G are shown in Fig. 8(b), and the Ekman layers and associated Ekman pumping are very evident. The case of $B_0 = 0.1$ G, which is steady, is shown for comparison in Fig. 8(a). The Ekman number for the case of $B_0 = 0.5$ G is $\text{Ek} = \nu/R(u_\theta)_{\text{max}} \approx 3 \times 10^{-4}$, which is smaller than the critical value at which the sidewall boundary layer is thought to go unstable to a centrifugal instability [14]. It is not surprising, therefore, that this flow exhibits some unsteadiness, though it is remarkable that an external magnetic field as weak as the earth's field can destabilize the flow.

Figure 9 shows the velocity field in a vertical plane at four consecutive times for the case of $B_0 = 0.5$ G. Taylor vortices which have resulted from the centrifugal instability are evident near the sidewall, and the unsteadiness is associated with these toroidal vortices rolling up and down the cylindrical sidewall with a period of $T \approx 300$ s, while drifting in the azimuthal direction. (See, also, the movies in the Supplemental Material [17].) The four snapshots are separated by the time interval $T/4$.

The nonaxisymmetric nature of the flow is evident from Fig. 10, which shows, on the left, snapshots of the magnitude of the vertical velocity on a cylindrical surface located at $r/R = 0.972$, and on the right, snapshots of the vertical velocity across a horizontal cross section located at $z/d = 0.23$ [indicated by the horizontal line on the left of Fig. 10(a)]. The times of the snapshots are the same as for Fig. 9, i.e., separated by time intervals of $\sim T/4$. The azimuthal wave number of the drifting motion is $m = 4$.

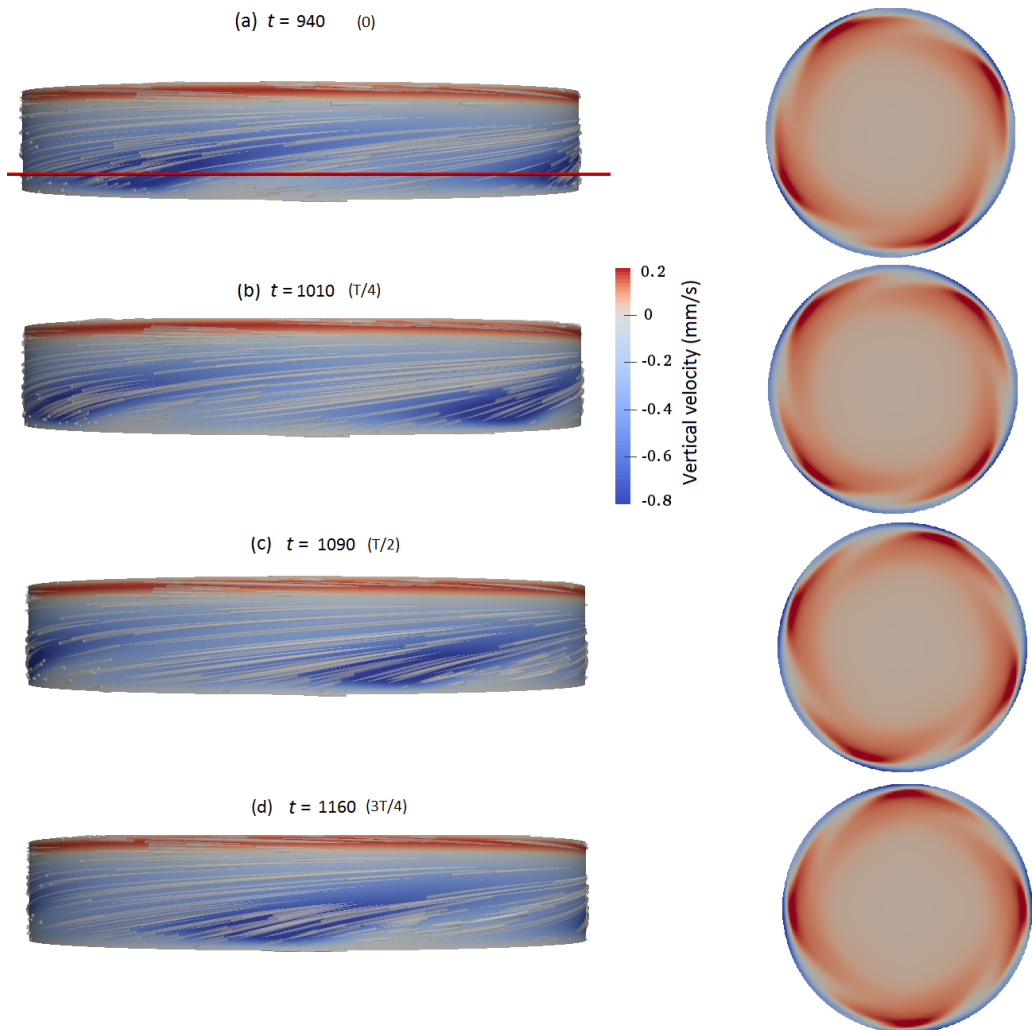


FIG. 10. The vertical velocity, for $B_0 = 0.5$ G, at $r/R = 0.972$ (left) and on the horizontal plane $z/d = 0.23$ (right) at (a) $t = 940$ s, (b) $t = 1010$ s, (c) $t = 1090$ s, and (d) $t = 1160$ s.

C. Results of the simulations for larger B_0 and the emergence of turbulence

According to (26), the azimuthal velocity should increase with B_0 according to $(u_\theta)_{\max} \sim B_0^{2/3}$ in a steady flow, and we have already suggested that this might also be true of the time-averaged velocity in an unsteady flow. Figure 11 shows the computed maximum of the time-averaged azimuthal velocity, $\langle u_\theta \rangle_{\max}$, driven by the force distribution (9), as a function of B_0 . It is clear that, despite the unsteadiness at $B_0 = 0.5$ G and $B_0 = 0.8$ G, the scaling law $(u_\theta)_{\max} \sim B_0^{2/3}$ is indeed satisfied for those cases. There is a clear discrepancy, however, for the case of $B_0 = 1.5$ G, which suggests that the exponent q in the scaling $(u_\theta)_{\max} \sim B_0^q$ may be somewhat lower than $2/3$ for turbulent flow. Indeed, the exponent $q = 5/9$ has been suggested for fully developed turbulence [12].

Figure 12 shows the instantaneous (at $t = 1500$ s) and time-averaged azimuthal velocity on the planes $z/d = 0.23$ (left) and midplane (right) for the case of $B_0 = 1$ G. The computed flows

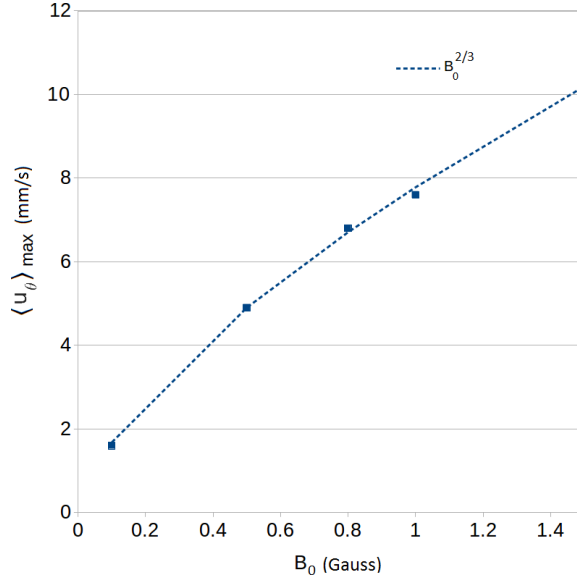


FIG. 11. The maximum time-averaged azimuthal velocity as a function of B_0 (in gauss) for the field strengths $B_0 = 0.1$ – 1.5 G. The dotted line is $B_0^{2/3}$.

correspond to the force distributions (9) (i.e., the true force distribution) and (14) with $p = 6$ (an approximation to the depth-averaged force). The theoretical prediction (23) is also shown. Once again, it is clear that (i) the azimuthal velocity in the core is more or less independent of depth, (ii) the true and depth-averaged force distributions produce essentially the same azimuthal velocity, and (iii) the theoretical estimate is an excellent fit to the computed flow.

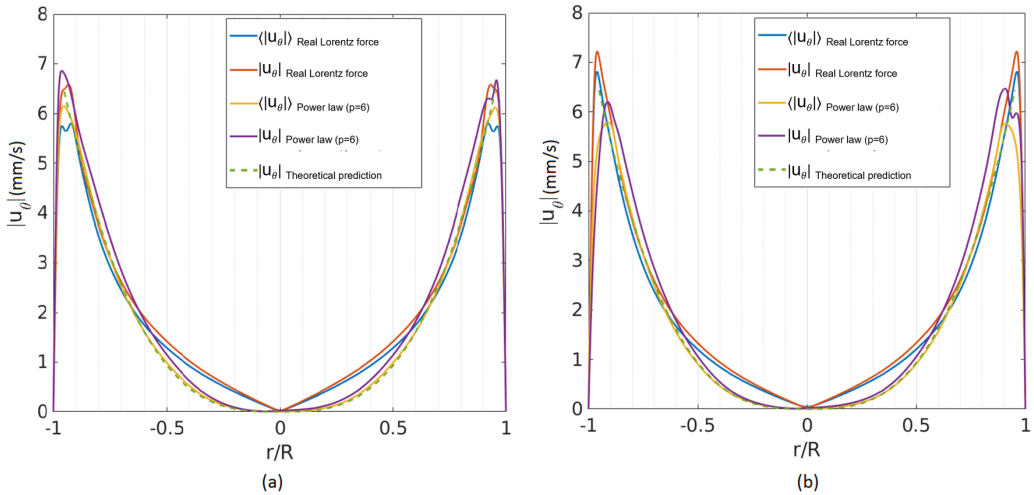


FIG. 12. The instantaneous and time-averaged azimuthal velocity on the planes $z/d = 0.23$ (left) and midplane (right) for $B_0 = 1$ G. The computed flows correspond to the full force distribution [Eq. (9), blue and red] and the power-law approximation [Eq. (14)] with $p = 6$ (yellow and purple). The theoretical prediction of Eq. (23) is also shown (green, dashed). The symbol $\langle \rangle$ denotes a time average.

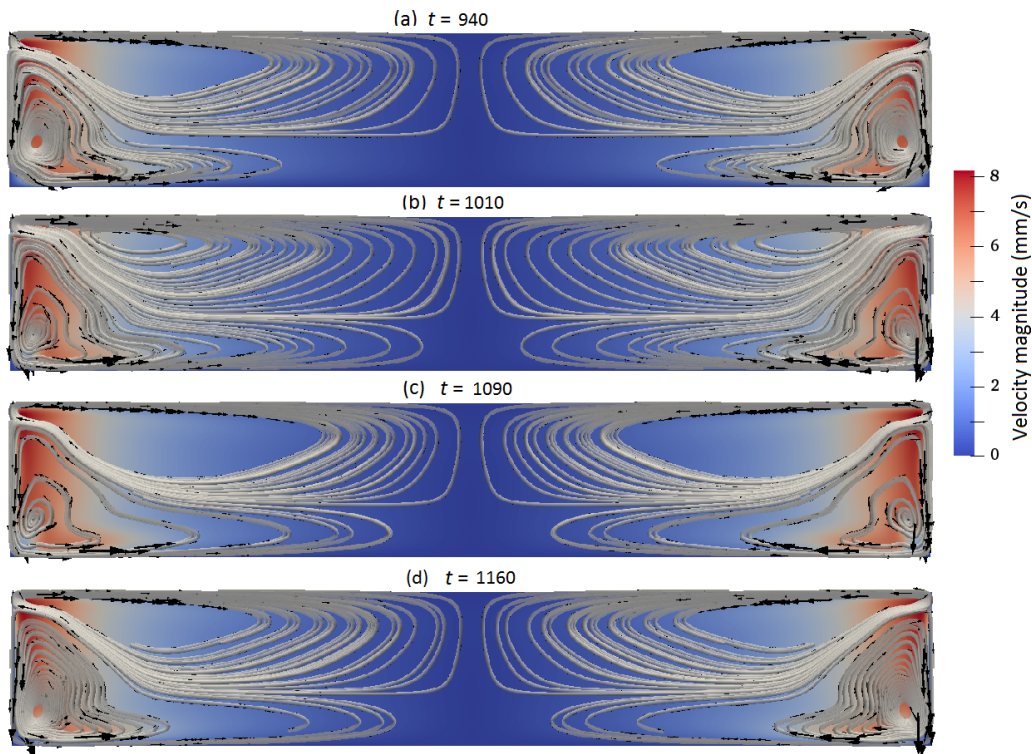


FIG. 13. The instantaneous velocity magnitude, $|\mathbf{u}|$, and streamlines in a vertical plane, for $B_0 = 1$ G. The times are (a) $t = 940$ s, (b) $t = 1010$ s, (c) $t = 1090$ s, and (d) $t = 1160$ s.

The time-averaged flow pattern does not change very much as B_0 increases from 0.1 to 1.5 G. What does change, however, is the degree of unsteadiness, which becomes more severe as the forcing increases and the Ekman number, $\text{Ek} = \nu/R(u_\theta)_{\max}$, falls. Consequently, we shall now focus on that unsteadiness.

Figure 13 shows the instantaneous velocity magnitude, $|\mathbf{u}|$, and the streamlines in a vertical plane, for the case of $B_0 = 1$ G and at the times $t = 940$ s, 1010 s, 1090 s, and 1160 s. These are the same times as in Figs. 9 and 10. Once again, Taylor vortices are evident near the sidewall, and the unsteadiness is, in part, associated with these toroidal vortices rolling up and down the cylindrical sidewall while drifting in the azimuthal direction. (See, also, the movies in the Supplemental Material [17].) However, the flow is now weakly turbulent, which also contributes to the unsteadiness.

The nonaxisymmetric nature of the flow and the azimuthal drifting of the mean flow pattern are evident from Fig. 14. This shows, on the left, snapshots of the magnitude of the vertical velocity on a cylindrical surface located at $r/R = 0.972$, and on the right, snapshots of the vertical velocity across a horizontal plane located at $z/d = 0.23$. Once again, the azimuthal wave number of the drifting motion is $m = 4$.

The rise in unsteadiness with increasing B_0 and the eventual emergence of weak turbulence are illustrated by Fig. 15. This shows a time series of $|\mathbf{u}|$ for $B_0 = 0.5, 0.8, 1.0$, and 1.5 G at the locations (a) $r/R = 0.972, z/d = 0.23$ and (b) $r/R = 0.972, z/d = 0.5$. The location $r/R = 0.972$ was chosen as the fluctuations resulting from the unsteady Taylor vortices are largest at this radius. In all cases there is an initial transient as the flow spins up from rest. After this transient, the time series for $B_0 = 0.5$ G, as well as for $B_0 = 0.8$ G, show that the flow is unsteady but laminar, with one dominant frequency in both cases, and a second weaker oscillation evident in the case of $B_0 = 0.8$ G.

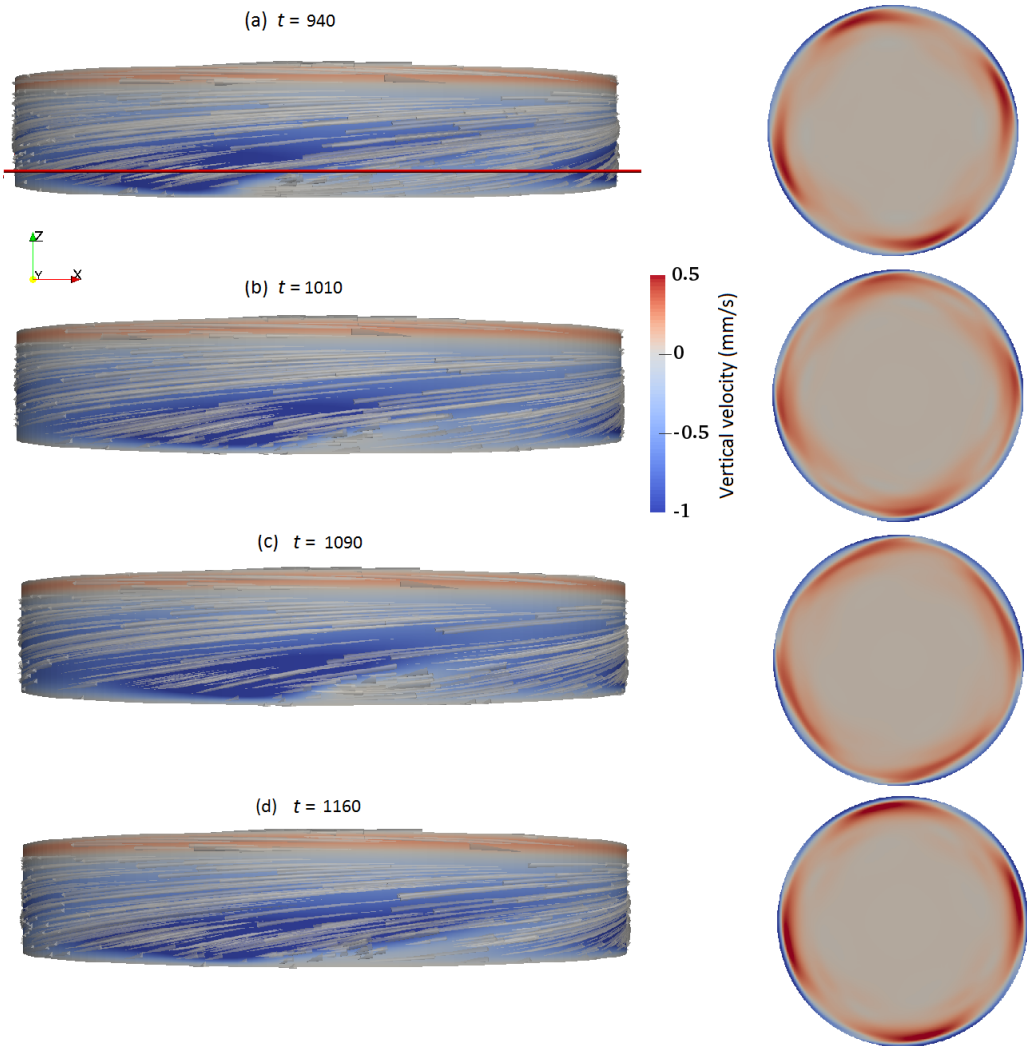


FIG. 14. The vertical velocity at $r/R = 0.972$ (left) and on the horizontal plane $z/d = 0.23$ (right) for $B_0 = 1$ G and at times (a) $t = 940$ s, (b) $t = 1010$ s, (c) $t = 1090$ s, and (d) $t = 1160$ s.

Although the flow patterns are similar for $B_0 = 0.5$ G and $B_0 = 1.0$ G, as seen from a comparison of Figs. 9 and 13, Fig. 15 shows that weak turbulence, or at the very least chaotic fluctuations, have developed in the case of $B_0 = 1.0$ G. This is even more evident for $B_0 = 1.5$ G, where the turbulence is clearer. It is surprising that a magnetic field not much larger than that of the earth can drive such a turbulent flow.

Finally, Fig. 16 shows a time series of the velocity magnitude at different radii, $r/R = 0.78, 0.89,$ and 0.972 , all for the same height, $z/d = 0.23$. The three panels correspond to (a) $B_0 = 0.5$ G, (b) $B_0 = 0.8$ G, and (c) $B_0 = 1.0$ G. Following the transient, in all three cases the fluctuations increase markedly with radius, indicating that the unsteady Taylor vortices dominate the unsteadiness. Indeed, there are almost no fluctuations at all for $r/R < 0.78$ in all three cases. The weak turbulence in the case of $B_0 = 1.5$ G is also restricted to large radii.

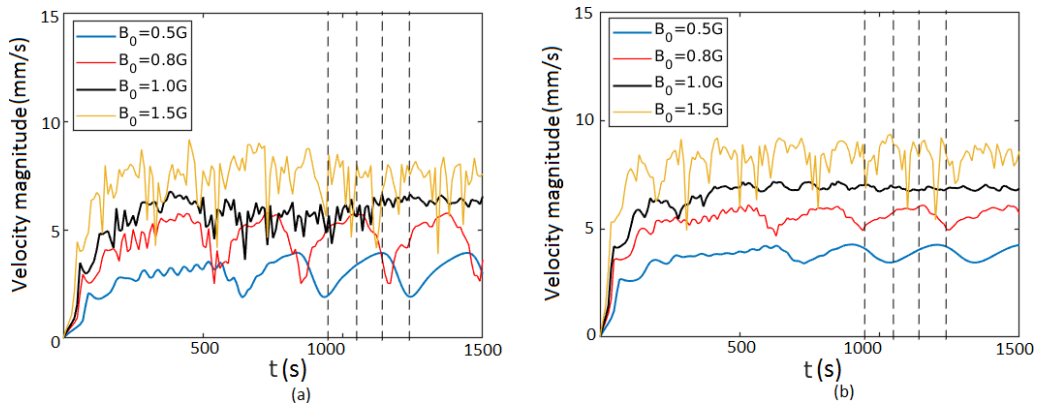


FIG. 15. Time series of $|\mathbf{u}|$ at (a) $z/d = 0.23$ and (b) $z/d = 0.5$ for $B_0 = 0.5, 0.8, 1.0,$ and 1.5 G at the radius $r/R = 0.972$. Dashed lines show the times in Figs. 9, 10, 13, and 14.

V. DISCUSSION AND CONCLUSIONS

We have adapted the analytical model of [12] to laminar flow in a cylindrical liquid-metal battery with a practical geometry. Our simulations have shown that our analytical model is accurate, not only for steady flow ($B_0 = 0.1$ G), but also for the time-averaged velocity in an unsteady laminar flow ($B_0 = 0.5, B_0 = 0.8$ G) and in a weakly turbulent flow ($B_0 = 1.0$ G). This is clear from Figs. 6 and 12. However, Fig. 11 suggests that the exponent in the scaling law $u_\theta \sim F_\theta^{2/3} R/v^{1/3}$ may start to drift away from $2/3$ as the turbulence builds up, and indeed that was predicted in [12], who suggests that $2/3$ be replaced by $5/9$ for fully developed turbulence. The reason for the change in the scaling law is that the structure of the Ekman layers alters somewhat as we move from laminar to turbulent flow, although the basic flow structure and force balances all remain the same.

We have also shown that, for the limited range of B_0 considered here, the unsteadiness and weak turbulence is restricted, more or less, to the fluid adjacent to the outer radial boundary, where the flow is unstable to a centrifugal instability. This is unlikely to be true, however, for stronger forcing, where distributed turbulence would be expected.

However, our primary conclusion is that surprisingly weak magnetic fields are capable of destabilizing the flow and inducing turbulence, with turbulence first appearing at around $B_0 \sim 1.0$ G. By comparison, the earth's magnetic field at sea level is around 0.5 G, depending on the location. This extreme sensitivity of liquid-metal pools carrying a radial current to an external magnetic field has long been known in the context of vacuum-arc remelting, where great effort is made to minimize any vertical magnetic field (see [9], Chap. 12).

The fact that the destabilizing external field is very weak is important for battery design. While some motion is beneficial because of the mixing it produces (see [5,6,2]), too much can produce strong turbulence which could disrupt the interface between the thin electrolyte layer and the bismuth. It is important, therefore, that stray magnetic fields are controlled, and this, in turn, has implications for the electrical design of battery clusters.

ACKNOWLEDGMENTS

A.R. wishes to acknowledge the research funding from an IITB seed grant and a SERB SRG grant, and Strategic Partnerships Office, University of Cambridge for support through the award of the Cambridge-Hamied Visiting Fellowship.

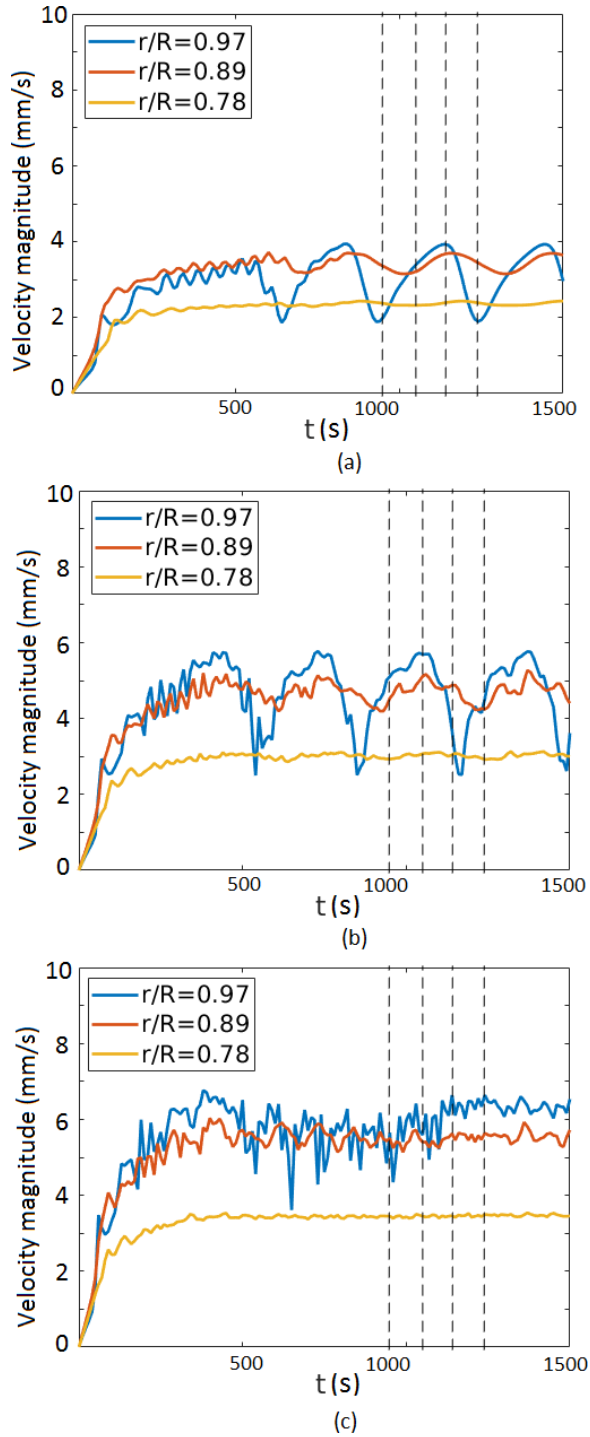


FIG. 16. Time series of $|\mathbf{u}|$ at the same height, $z/d = 0.23$, but at different radii, $r/R = 0.78, 0.89, 0.972$. (a) $B_0 = 0.5$ G, (b) $B_0 = 0.8$ G, and (c) $B_0 = 1.0$ G. The dashed lines show the times for Figs. 9, 10, 13, and 14.

- [1] D. H. Kelley and T. Weier, Fluid mechanics of liquid metal batteries, *Appl. Mech. Rev.* **70**, 020801 (2018).
- [2] P. Personnetaz, T. S. Klopper, N. Weber, and T. Weier, Layer coupling between solutal and thermal convection in liquid metal batteries, *Int. J. Heat Mass Transfer* **188**, 122555 (2022).
- [3] R. F. Ashour, D. H. Kelley, A. Salas, M. Starace, N. Weber, and T. Weier, Competing forces in liquid metal electrodes and batteries, *J. Power Sources* **378**, 301 (2018).
- [4] W. Herreman, C. Nore, P. Ziebell Ramos, L. Cappanera, J.-L. Guermond, and N. Weber, Numerical simulation of electrovortex flows in cylindrical fluid layers and liquid metal batteries, *Phys. Rev. Fluids* **4**, 113702 (2019).
- [5] N. Weber, M. Nimtz, P. Personnetaz, T. Weier, and D. Sadoway, Numerical simulation of mass transfer enhancement in liquid metal batteries by means of electro-vortex flow, *J. Power Sources Adv.* **1**, 100004 (2020).
- [6] W. Herreman, C. Nore, L. Cappanera, and J.-L. Guermond, Efficient mixing by swirling electrovortex flows in liquid metal batteries, *J. Fluid Mech.* **915**, A17 (2021).
- [7] X. Ning, S. Phadke, B. Chung, H. Yin, P. Burke, and D. R. Sadoway, Self-heating Li-Bi liquid metal battery for grid-scale energy storage, *J. Power Sources* **275**, 370 (2015).
- [8] P. A. Davidson, D. Kinnear, R. Lingwood, D. J. Short, and X. He, The role of Ekman pumping in confined, axisymmetric flows driven by a prescribed Lorentz force, *Eur. J. Mec., B* **18**, 693 (1999).
- [9] P. A. Davidson, *Introduction to Magnetohydrodynamics*, 2nd ed. (Cambridge University Press, Cambridge, 2017).
- [10] I. Kolesnichenko, P. Frick, V. Eltishchev, S. Mandrykin, and F. Stefani, Evolution of a strong electrovortex flow in a cylindrical cell, *Phys. Rev. Fluids* **5**, 123703 (2020).
- [11] M. Abramowitz and I. A. Stegun, *Handbook of Mathematical Functions* (Dover, New York, 1965).
- [12] P. A. Davidson, Swirling flow in an axisymmetric cavity of arbitrary profile, driven by a rotating magnetic field, *J. Fluid Mech.* **245**, 669 (1992).
- [13] P. A. Davidson, *Incompressible Fluid Mechanics* (Oxford University Press, Oxford, 2021).
- [14] Ö. Savas, Spin-down to rest in a cylindrical cavity, *J. Fluid Mech.* **234**, 529 (1992).
- [15] H. Jasak, Error analysis and estimation for the finite volume method with applications to fluid flow, Ph.D. thesis, Imperial College of Science, Technology, and Medicine, 1996, pp. 146–152.
- [16] J. H. Ferziger and M. Peric, *Computational Methods for Fluid Dynamics*, 3rd ed. (Springer-Verlag, Berlin, 2002) p. 176.
- [17] See Supplemental Material at <http://link.aps.org/supplemental/10.1103/PhysRevFluids.7.074701> for movies corresponding to Figs. 9 and 13.